Nanoscale Advances

ROYAL SOCIETY OF CHEMISTRY

PAPER

View Article Online
View Journal | View Issue

Cite this: *Nanoscale Adv.*, 2025, **7**, 4129

CuNi–PTC metal–organic framework: unveiling pseudocapacitive energy storage and water splitting capabilities†

Samika Anand and Kalathiparambil Rajendra Pai Sunajadevi *

Received 31st March 2025
Accepted 9th May 2025

DOI: 10.1039/d5na00300h

rsc.li/nanoscale-advances

Metal–organic frameworks (MOFs), owing to their distinctive structural properties and customizable functionalities, have been garnering significant attention in the pursuit of advanced energy storage and conversion technologies. In this work, a bimetallic MOF, CuNi–PTC, has been synthesized through a straightforward method. Investigations reveal its potential as a high-performance electrode material for supercapacitors and as an electrocatalyst for water splitting. The CuNi–PTC MOF features a large specific surface area, hierarchical porosity, and strong structural stability, as evidenced by spectroscopic and electron microscopy analyses. As a supercapacitor electrode material, CuNi–PTC delivers an impressive specific capacitance of 1066.24 F g^{-1} at a current density of 1 A g^{-1}, along with excellent cycling stability, retaining 94% of its capacity after 5000 charge–discharge cycles. Additionally, the electrocatalytic performance of CuNi–PTC for both the hydrogen evolution reaction (HER) and the oxygen evolution reaction (OER) was assessed, showing overpotentials of 212 mV for the HER and 380 mV for the OER at a current density of 10 mA cm^{-2}, along with exceptional long-term durability.

Introduction

The rapid rise in global energy demand has underscored the urgent need for alternative energy solutions. Traditional energy sources, such as fossil fuels, are becoming increasingly unsustainable due to their limited reserves and harmful environmental impacts, including greenhouse gas emissions and pollution. This growing disparity between supply and demand has accelerated the search for cleaner and more sustainable energy options. Renewable energy sources, like solar, wind, and hydropower, are gaining prominence as promising alternatives to fossil fuels, as they rely on abundant resources and natural processes that are far less detrimental to the environment. However, these energy sources are not without challenges, particularly their intermittency, as energy generation can fluctuate based on external factors such as weather conditions and time of day.[1,2] As a result, the development of advanced energy storage systems has become critical to ensuring the reliability of renewable energy sources.

Energy storage technologies play a vital role in balancing the energy grid by capturing excess energy generated during periods of low demand and storing it for use when demand increases or when renewable energy production is low. This not only stabilizes the power grid system but also ensures a continuous and dependable energy supply. Technologies such as supercapacitors, batteries, and flow batteries are at the forefront of this effort, each offering distinct advantages.[3] Supercapacitors, known for their rapid energy discharge and recharging capabilities, along with their long cycle life, are particularly useful in applications where quick energy release is necessary.[4] At the same time, significant advances are being made in clean energy production technologies. One of the most promising methods is water splitting, a process that involves the electrochemical separation of water into hydrogen and oxygen. This is achieved through the hydrogen evolution reaction (HER) and the oxygen evolution reaction (OER), both of which are crucial for the production of clean hydrogen fuel.[5] Hydrogen, in turn, can be used in fuel cells for electricity generation or as a key feedstock in various industrial applications, making it an essential component in the transition to a low-carbon economy.[6] As such, developing efficient, durable, and cost-effective electrocatalysts for the HER and OER remains a central focus in the pursuit of scalable hydrogen production technologies.

The quest to enhance both energy storage and conversion technologies has led to an intense focus on improving electrode materials. These materials must exhibit high energy and power density, superior electrical conductivity, and long-term stability under operational conditions. Among the most promising materials being explored are Metal–Organic Frameworks (MOFs), which offer unique advantages in energy-related applications due to their highly tunable structures and exceptional porosity.[7–10] MOFs are crystalline materials formed due to coordination of metal ions or clusters with organic linkers,

Department of Chemistry, Christ University, Bengaluru 560029, Karnataka, India. E-mail: sunajadevi.kr@christuniversity.in

† Electronic supplementary information (ESI) available. See DOI: https://doi.org/10.1039/d5na00300h

resulting in versatile structures that can be customized for specific properties, including high surface areas, thermal and chemical stability, conductivity, and catalytic activity.[11,12] These characteristics make MOFs ideal candidates for applications in both energy storage devices, like supercapacitors, and energy conversion processes, such as water splitting.

Building on the potential of MOFs, recent attention has shifted towards bimetallic frameworks, which incorporate two different metal centers within the same structure. This dual-metal approach offers synergistic effects that often surpass the performance of their monometallic counterparts, by combining the distinct electronic, catalytic, or structural advantages of each metal.[13] Several bimetallic MOFs have demonstrated enhanced redox activity and stability in supercapacitive and electrocatalytic applications, attributed to improved electron transfer dynamics and optimized active site distribution.[14] Such frameworks are particularly appealing for multifunctional applications, where a single material is expected to operate efficiently in both charge storage and catalysis.[15] The rational design of bimetallic MOFs thus represents a powerful strategy for advancing next-generation energy materials.

This study focuses on the synthesis and characterization of a CuNi–PTC MOF, a bimetallic framework that incorporates copper (Cu) and nickel (Ni) metal centers, coordinated with perylene-3,4,9,10-tetracarboxylic dianhydride (PTC) as the organic linker. The synthesized MOF has been characterized using various spectroscopic and electron microscopy methods to evaluate its structure, crystallinity, and morphology. Following this, CuNi–PTC has been employed as an electrode material for supercapacitors and electrocatalytic water splitting, showcasing high specific capacitance, lower overpotential, and remarkable long-term stability. The combination of Cu and Ni in the framework is expected to offer enhanced electrochemical and catalytic performance. Copper, with its excellent conductivity and catalytic properties, is complemented by nickel, which is known for its stability and efficiency in catalytic reactions. The bimetallic nature of this MOF is anticipated to provide a synergistic effect, improving its overall performance.

Experimental

Materials

All chemicals were used as received, adhering to established purity standards. Perylene-3,4,9,10-tetracarboxylic dianhydride (PTC) was sourced from Lancaster Synthesis, while nickel nitrate ($Ni(NO_3)_2 \cdot 6H_2O$) and cupric acetate ($Cu(OAc)_2 \cdot H_2O$) were obtained from Sigma-Aldrich.

Synthesis of CuNi–PTC

The CuNi–PTC MOF was synthesized under solvothermal conditions using a conventional heating approach with DMF as the solvent.[16] Initially, PTC was converted into its potassium salt (K_4PTC) by refluxing it with 4.5 equivalents of KOH for 12 h, yielding a fluorescent green solution. This solution was slowly added to acetone, leading to the formation of a yellow precipitate. The precipitate was filtered, thoroughly washed with acetone, and dried in a hot air oven to obtain K_4PTC.[17] For the synthesis of CuNi–PTC, aqueous solutions of K_4PTC (0.2 mmol in 2 mL water), $Ni(NO_3)_2 \cdot 6H_2O$ (0.1 mmol in 2 mL water), and $Cu(OAc)_2 \cdot H_2O$ (0.1 mmol in 2 mL water) were sonicated separately for 30 minutes. These solutions were then combined and stirred with 11 mL of DMF for 3 hours using a magnetic stirrer. The mixture was transferred into an autoclave and heated in a muffle furnace at 180 °C for 24 h. After cooling, the resulting precipitate was filtered, thoroughly washed with water and ethanol, and dried to yield a brownish powder of CuNi–PTC.

Characterization techniques

The synthesized MOF, CuNi–PTC, was thoroughly characterized using a variety of spectroscopic and electron microscopy techniques to confirm its crystallinity and examine its structure, bonding, and morphology. X-ray diffraction (XRD) was conducted with a Rigaku Smart Lab diffractometer, using Cu Kα radiation ($\lambda = 0.154$ nm), to assess the crystalline properties of the MOF. Functional group identification was performed through Fourier transform infrared (FTIR) spectroscopy using a Shimadzu IR Spirit-L spectrometer. X-ray photoelectron spectroscopy (XPS) was performed with a PHI VERSAPROBE III system to analyze bonding characteristics and confirm the elemental composition of the MOF. Thermal stability was evaluated *via* thermogravimetric analysis (TGA) on a PerkinElmer analyzer. The Brunauer–Emmett–Teller (BET) method was employed to determine the surface area and pore size using a BELSORP-mini II surface area analyzer. Field emission scanning electron microscopy (FESEM), combined with energy-dispersive X-ray spectroscopy (EDS), was performed with a Carl Zeiss Supra 55 microscope to investigate the material's morphology and composition. Additionally, a Zeta-20 KLA Tencor optical profilometer was used to capture the three-dimensional profile of the MOF.

Electrochemical analysis

An electrochemical workstation, CHI608E (CH Instruments Inc., USA), equipped with a three-electrode setup, was employed for electrochemical studies. Supercapacitor performance was assessed using a saturated calomel electrode as the reference, a platinum wire as the counter electrode, and a working electrode consisting of the prepared sample coated on nickel foam. The electrolyte used was 3 M KOH. The working electrode was fabricated by drop-casting an aqueous slurry of the sample, which was prepared by mixing 1 g of the MOF with 0.289 g of activated carbon, 0.0938 g of PVDF, and 60 μL of NMP, onto Ni foam, followed by overnight drying. Cyclic voltammetry (CV), galvanostatic charge–discharge (GCD), and electrochemical impedance spectroscopy (EIS) were employed at room temperature to assess the supercapacitor behavior of the prepared sample. The specific capacitance (C_s), energy density (E), and power density (P) were calculated using eqn (1)–(3), respectively.

$$C_s = \frac{I \times \Delta t}{m \times V} \quad (1)$$

$$E = \frac{C_s \times V^2}{2 \times 3.6} \quad (2)$$

$$P = \frac{E \times 3600}{\Delta t} \quad (3)$$

Water splitting experiments were performed using an electrochemical cell with a three-electrode configuration, comprising a working electrode, a calomel reference electrode, and a platinum wire counter electrode, with 1 M KOH as the electrolyte. The working electrode was prepared by drop-casting catalyst ink, which was made by mixing 50 mg of the synthesized MOF, 20 mg of PVDF, 60 μL of ethanol, and 60 μL of water, onto nickel foam, followed by drying overnight at 60 °C. The electrochemical analysis involved cyclic voltammetry (CV), linear sweep voltammetry (LSV), and electrochemical impedance spectroscopy (EIS). LSV was conducted at a scan rate of 5 mV s^{-1}, and the overpotentials were determined at a current density of 10 mA cm^{-2}. The potential (V *vs.* RHE) was calculated using eqn (4).

$$E(V\ vs.\ \mathrm{RHE}) = E + (0.0591 \times \mathrm{pH}) + 0.241 \quad (4)$$

Results and discussion

Structural and morphological examination of CuNi–PTC

The X-ray diffraction (XRD) analysis of the synthesized K_4PTC and CuNi–PTC is depicted in Fig. 1a. The XRD pattern for K_4PTC shows distinct diffraction peaks at 2θ angles of 6.6°, 13.1°, 26.1°, 30.1°, 32.4°, and 39.2° corresponding to the Miller indices (*hkl*) of (001), (110), (202), (122), (204), and (222) planes, respectively.[18,19] CuNi–PTC exhibits peak positions similar to those of K_4PTC, but with differences in intensity and slight shifts in certain planes, indicating the successful formation of CuNi–PTC. The sharp and well-defined peaks reflect its crystallinity and the high degree of order in the framework. Additionally, while some extra reflections are observed, these are attributed to reorganization owing to framework formation leading to new crystalline phases or partial recrystallization effects, rather than impurity phases. Notably, the characteristic diffraction peaks of nickel oxide, typically found at 2θ values around 37.3° and 43.3°, and copper oxide centred at 2θ values around 35.6° and 38.3° are absent in the CuNi–PTC pattern.[20,21] This absence confirms the successful synthesis of CuNi–PTC without residual nickel oxide or copper oxide phases, ensuring the purity of the material.

Fig. 1b shows the Fourier Transform Infrared (FTIR) spectra for CuNi–PTC and K_4PTC, offering insights into the bonding characteristics of these materials. The peaks at 1348 cm^{-1} and 1564 cm^{-1} are attributed to the symmetric and asymmetric stretching vibrations of the carboxylate group ($-COO^-$), consistent with similar observations in related studies.[22] A significant feature in the CuNi–PTC spectrum is the shift in the carbonyl (C=O) stretching vibrations, typically found around 1700 cm^{-1}, to a lower frequency of 1676 cm^{-1}, indicating the coordination of the carboxylate group to the Cu^{2+} and Ni^{2+} ions.[23,24] This weakens the carbonyl bond, resulting in a reduced stretching frequency, and confirms the strong interaction between the carboxylate group of the ligand and the metal center, validating the metal–ligand binding.

Additionally, the spectra exhibit peaks at 1271 cm^{-1}, 1048 cm^{-1}, and 817 cm^{-1} corresponding to C–C stretching, C–O stretching, and C–H bending vibrations, respectively, within the ligand's aromatic ring.[25] The broad peak around 3450 cm^{-1} is attributed to O–H stretching, likely due to the presence of trace amounts of water during the crystallization process. In the lower frequency range (400 to 800 cm^{-1}), distinct peaks provide further evidence of metal–ligand interactions. Most notably, the peaks at 454 cm^{-1}, 650 cm^{-1}, and 740 cm^{-1} are associated with Ni–O and Cu–O stretching vibrations,[26,27] confirming the coordination between Cu^{2+}/Ni^{2+} ions and the oxygen atoms of the ligand in CuNi–PTC.

X-ray photoelectron spectroscopy (XPS) was conducted to analyze the bonding within the as synthesized CuNi–PTC framework. Fig. 2a depicts the survey spectrum of CuNi–PTC showing the presence of peaks centered at 284.9, 531.8, 856.3,

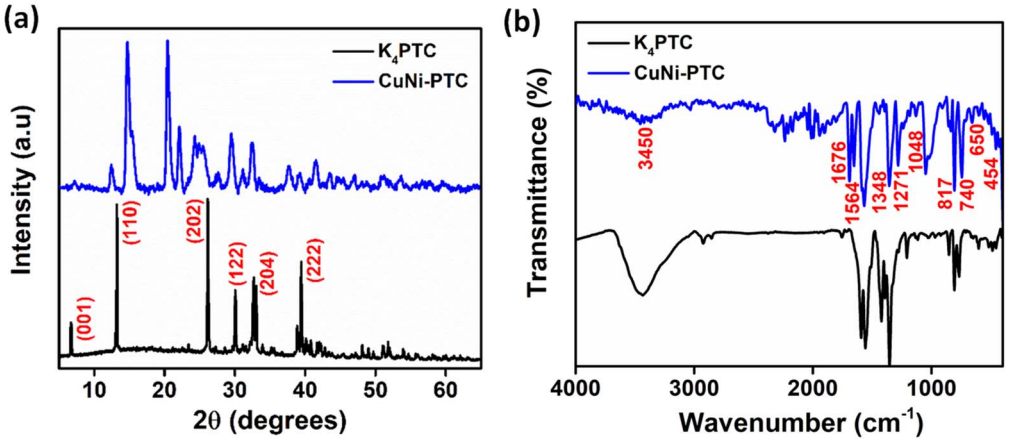

Fig. 1 (a) X-ray diffractogram and (b) FTIR spectra of K_4PTC and CuNi–PTC.

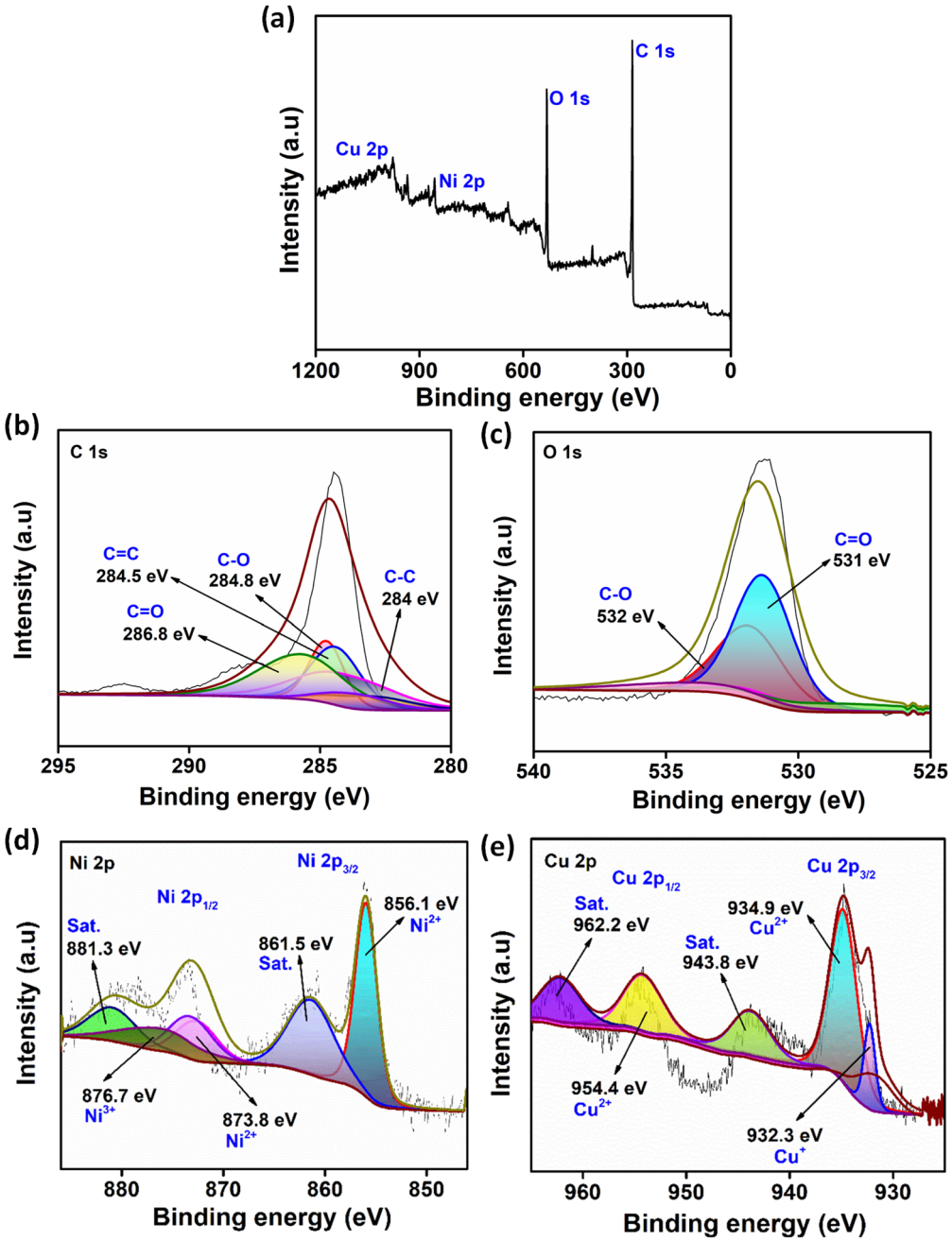

Fig. 2 (a) XPS survey spectrum of CuNi–PTC. High-resolution core spectra of (b) C 1s, (c) O 1s, (d) Ni 2p, and (e) Cu 2p.

and 934.9 eV corresponding to C 1s, O 1s, Ni 2p, and Cu 2p with atomic percentages of 76.7%, 20.6%, 1.67%, and 1.07%, respectively. Additionally, high-resolution profiles of the respective elements were further interpreted to corroborate their bonding environment within the framework. Fig. 2b shows the high-resolution scan for C 1s. The spectrum shows peaks around 284 eV and 284.5 eV, which correspond to sp^3 carbon (C–C bonds) and sp^2 carbon (C=C) from aromatic rings in the PTC ligand of the MOF. Moreover, peaks centered at 284.8 eV and 286.8 eV are attributed to C–O and C=O linkages in the PTC linker structure.[28] The O 1s spectrum (Fig. 2c) depicts two peaks, at 531 eV and 532 eV, owing to the presence of C=O and C–O linkages in the PTC linker.

The Ni 2p spectrum (Fig. 2d) displays two prominent peaks corresponding to the $2p_{3/2}$ and $2p_{1/2}$ spin–orbit levels. The peaks at 856.1 eV and 873.8 eV are assigned to Ni^{2+} $2p_{3/2}$ and Ni^{2+} $2p_{1/2}$, respectively. These primary peaks are further accompanied by characteristic satellite features, with distinct peaks observed at 861.5 eV and 881.3 eV. A low intensity peak at 876.7 eV is attributed to the presence of trace amounts of Ni^{3+}.[29,30] This suggests that, while Ni^{2+} is the dominant oxidation state, there is a degree of oxidation state heterogeneity within the material. The Ni^{3+} species reflect a small but

significant deviation from the predominant Ni^{2+} state, potentially resulting from local structural variations or partial oxidation, and may influence the overall electronic properties of the MOF.

The Cu 2p spectrum (Fig. 2e) reveals multiple peaks corresponding to the $2p_{3/2}$ and $2p_{1/2}$ spin–orbit levels, indicative of copper's oxidation states. The main peak at 934.9 eV is attributed to the Cu^{2+} $2p_{3/2}$ transition, suggesting the presence of Cu(II) species. In contrast, a low intensity peak at 932.3 eV corresponds to the Cu^{+} $2p_{3/2}$ state. Additionally, a satellite peak is observed at 943.8 eV, which is a hallmark of the Cu^{2+} oxidation state. The higher energy $2p_{1/2}$ level appears at 954.4 eV, corresponding to the Cu^{2+} $2p_{1/2}$ transition, with a satellite peak at 962.2 eV, further reinforcing the presence of Cu^{2+}.[31,32] This combination of Cu(I) and Cu(II) states highlights the mixed oxidation states of copper in the material, which could play a critical role in defining the MOF's electronic and catalytic properties. The heterogeneity of copper's oxidation states suggests varying local environments, possibly influenced by coordination with the PTC ligands or surrounding Ni metal nodes.

The FESEM images depict the morphology of CuNi–PTC comprising Cu and Ni as metal nodes (Fig. 3a and b). The structure exhibits a combination of distinct plate-like structures and smoother flake formations, which can be correlated with the reported characteristics of Cu–PTC and Ni–PTC, respectively. The larger, sharper-edged plates observed in the image are consistent with the morphology typically associated with Cu MOFs, where the Cu nodes tend to form rigid, plate-like assemblies. Meanwhile, the smoother, less angular flake-like structures are likely indicative of the Ni metal nodes, which have been reported to form more refined and continuous surfaces in MOFs. This combination of textures highlights the distinct contributions of both metals to the overall morphology of the as synthesized MOF, reflecting their individual structural tendencies within the framework. Fig. S1† depicts the EDS spectrum of the realized MOF showcasing the distribution of elements C, O, Cu, and Ni in 68.92, 21.93, 5.56, and 4.19 weight (wt)%, respectively. Fig. 3c presents a three-dimensional (3D) surface view of CuNi–PTC, obtained through optical profilometry. This 3D surface profile provides a comprehensive depiction of the material's topography, revealing variations in surface roughness. The uneven surface, characterized by micro and nanoscale cavities, enhances ion accessibility to the electrode material, promoting more efficient ion diffusion and lowering charge transfer resistance.[33] The average surface roughness (S_a) and root mean square roughness (S_q) for the MOF were measured at 4.526 μm and 5.754 μm, respectively.

The thermogram of the synthesized MOF reveals a multi-step thermal degradation pattern, indicative of its structural integrity and stability under heat (Fig. 4a). The first stage, exhibiting approximately 10% weight loss up to 120 °C, corresponds to the

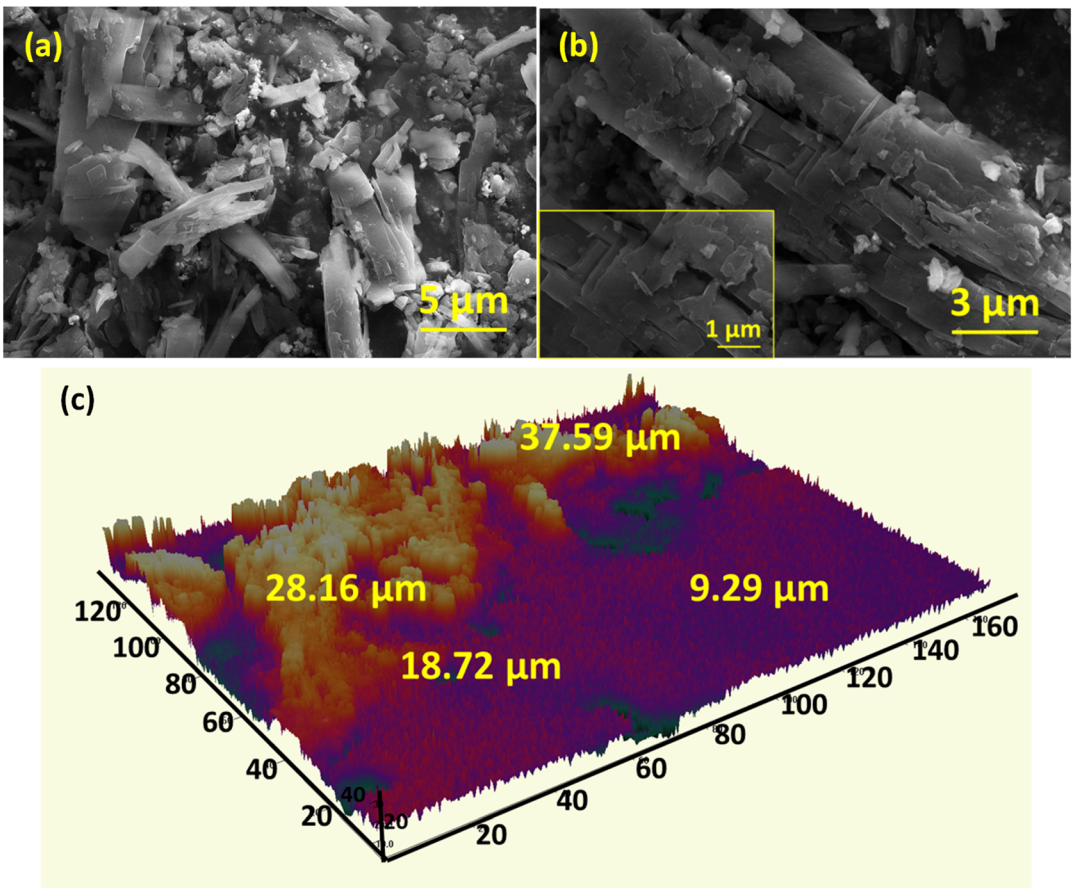

Fig. 3 (a and b) FESEM micrographs and (c) 3D surface profile of CuNi–PTC.

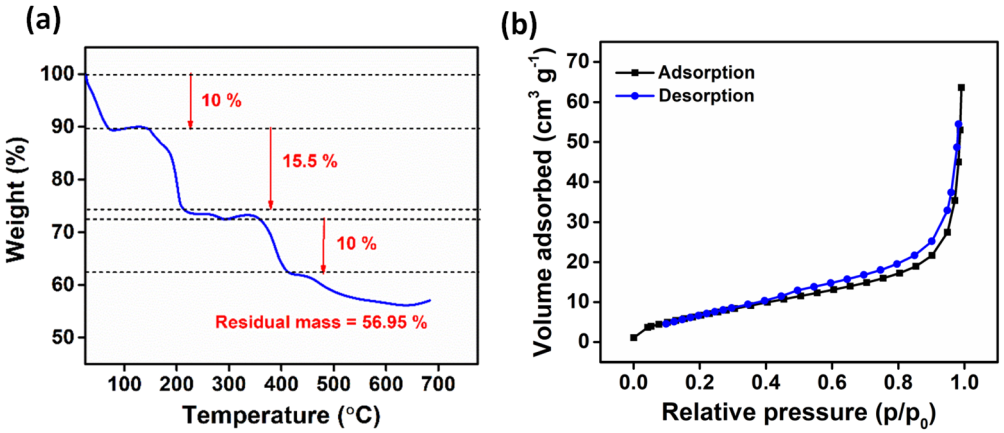

Fig. 4 (a) Thermogram and (b) N_2 adsorption–desorption isotherm of CuNi–PTC.

evaporation of physically adsorbed water or residual solvents within the porous structure. As the temperature increases to the range of 150 °C to 200 °C, a more pronounced weight loss of 15.5% is observed, which likely results from the release of coordinated H_2O attached to the framework. Finally, a third decomposition event occurs between 350 °C and 400 °C, where a 10% weight loss is attributed to the breakdown of the coordination between the PTC linker and metal nodes, resulting in the release of volatile components like CO_2. Overall, the TGA profile suggests that the MOF demonstrates moderate thermal stability, leaving behind a residual mass of 56.95% at 700 °C.

The Brunauer–Emmett–Teller (BET) surface area and pore volume of the synthesized CuNi-MOF were determined from N_2 adsorption–desorption isotherms recorded at 77 K. The isotherm, shown in Fig. 4b, exhibits characteristics of a type III isotherm, which is indicative of multilayer adsorption, even at low relative pressures. The BET method was applied to calculate the surface area, yielding a value of 28.257 $m^2\ g^{-1}$. Notably, a hysteresis loop was observed in the relative pressure range of 0.0 to 1.0, particularly prominent at both low and high pressures. This loop corresponds to H1-type hysteresis, which is often linked to uniform pore structures and suggests the occurrence of capillary condensation within the material's mesopores.[34]

Further pore size distribution analysis, conducted using the Barrett–Joyner–Halenda (BJH) method and presented in Fig. S2,† indicated a total pore volume of 0.095 $cm^3\ g^{-1}$. The BJH analysis revealed a narrow pore size distribution, primarily pointing to the presence of micropores and mesopores. The pore diameter and average pore diameter identified through the BJH plot were 2.00 nm and 45.55 nm, confirming the material's classification as mesoporous.

Electrochemical investigation

The CuNi–PTC framework comprises repetitive Cu and Ni metal nodes interconnected with the organic ligand PTC through coordination bonds. The rigid planar structure and extended conjugation of the PTC ligand provide a stable and conductive backbone, promoting efficient electron transfer. Furthermore, the incorporation of both Cu and Ni metal nodes imparts distinct redox properties, creating a synergistic effect that enhances the composite's electrocatalytic activity and charge storage capacity. The bimetallic framework also increases the density of active sites, further improving electrochemical performance.

Considering these structural and compositional advantages, the electrochemical behavior of CuNi–PTC was systematically investigated using a conventional three-electrode cell configuration. The analysis involved cyclic voltammetry (CV), galvanostatic charge/discharge (GCD) experiments, linear sweep voltammetry (LSV), and electrochemical impedance spectroscopy (EIS) to assess its supercapacitive and water-splitting capabilities.

Importantly, the chemical stability of MOFs in acidic or basic media is a key determinant of their long-term viability in electrocatalytic systems. MOFs constructed from high-valent metal ions (*e.g.*, Zr^{4+} and Al^{3+}) and hard base ligands like carboxylates typically exhibit enhanced stability in acidic environments due to strong metal–ligand interactions.[35] Conversely, MOFs incorporating divalent transition metals (*e.g.*, Zn^{2+} and Co^{2+}) with nitrogen-donor ligands often show greater resistance in basic media,[36] as explained by the hard and soft acids and bases (HSAB) theory. According to this theory, strong soft acid–soft base interactions provide chemical robustness under alkaline conditions.[37]

In this context, CuNi–PTC may benefit from the strong coordination between Cu^{2+}/Ni^{2+} and the tetracarboxylate PTC ligand, along with structural reinforcement from its bimetallic nature. This combination is expected to show resilience in a basic medium as an electrolyte (KOH). This is further supported by the preserved morphology of the framework after several charge–discharge cycles in supercapacitance as well as prolonged electrolysis in water splitting, as discussed in the further sections.

Supercapacitance investigation

Fig. 5a and S3a† present the cyclic voltammograms of CuNi–PTC measured within the potential window of 0.1–0.5 V at

varying scan rates, ranging from 200 mV s^{-1} to 10 mV s^{-1}, and 10 mV s^{-1} to 1 mV s^{-1}, respectively. Notably, the CV curve recorded at a scan rate of 10 mV s^{-1} shows two distinct peaks at 0.169 V and 0.282 V, corresponding to cathodic reduction and anodic oxidation processes. The CV curves feature two prominent peaks, indicating that faradaic reactions are occurring within the material, which suggests that CuNi–PTC exhibits pseudocapacitive behavior due to redox processes rather than purely electrostatic charge storage, as is typical in double-layer capacitors. As the scan rate increases, the current

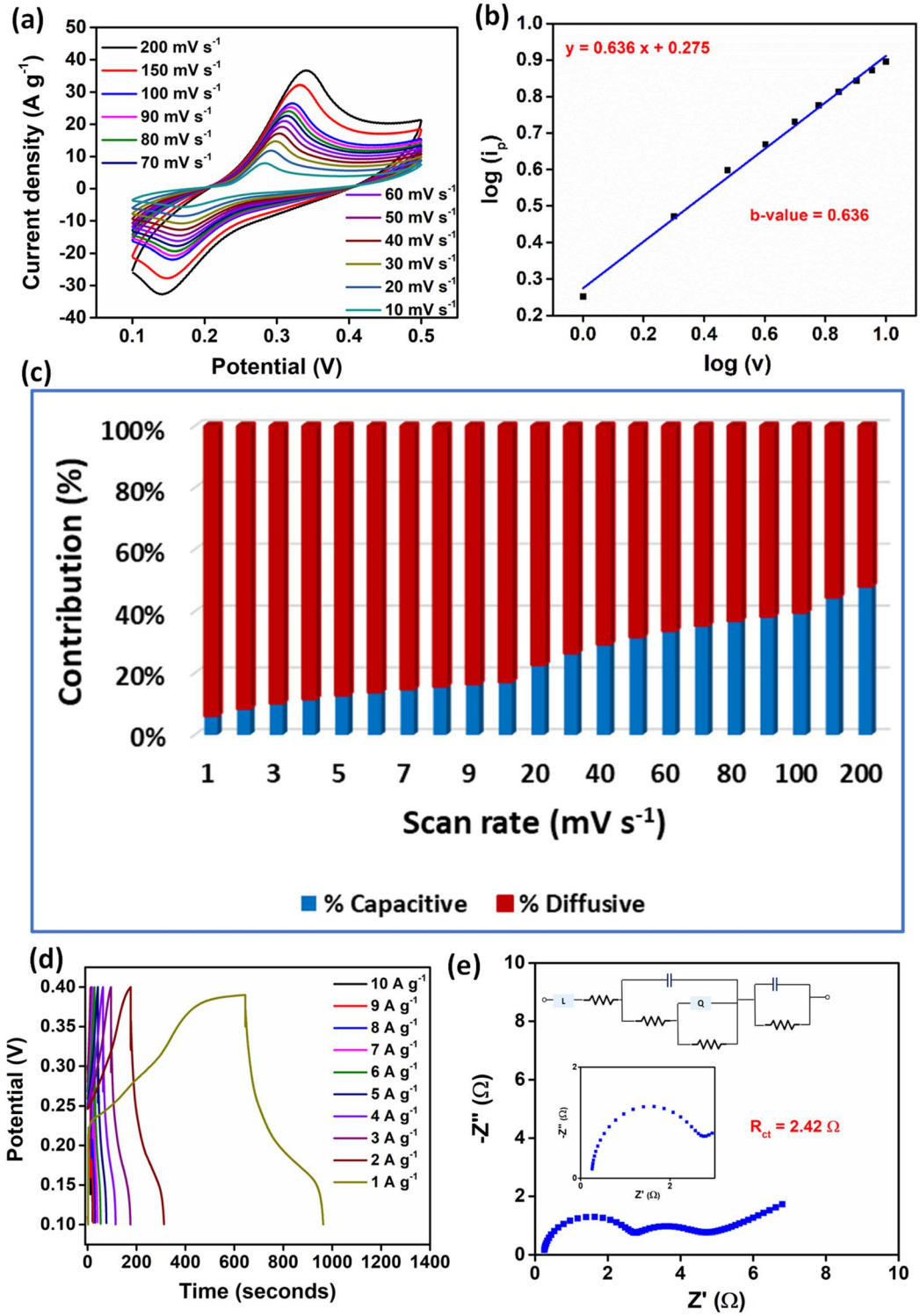

Fig. 5 (a) Cyclic voltammograms of CuNi–PTC. (b) Linear plot of log(i_p) *vs.* log(v). (c) Representation of capacitive and diffusive current contributions. (d) GCD curves. (e) Nyquist plot.

density rises accordingly, leading to an expansion of the CV curve area. This can be attributed to the reduced thickness of the electrolyte diffusion layer at higher scan rates, which facilitates faster ion exchange and electron transfer, resulting in an enhanced current response. Fig. S3b† compares the CV of the working electrode with bare Ni foam (also at 10 mV s^{-1}), clearly demonstrating the negligible redox activity of bare Ni foam. This comparison highlights the significant role of CuNi–PTC in contributing to the observed redox behavior.

To further substantiate these findings, the *b*-value was calculated from the slope of the $\log(i_p)$ *versus* $\log(v)$ plot, using the Randles–Ševčik equation (eqn (5)).[38]

$$i_p = av^b \quad (5)$$

For CuNi–PTC, the calculated *b*-value was 0.636 (Fig. 5b). This intermediate value, between 0.5 and 1, suggests that the charge storage mechanism involves a combination of surface-controlled capacitive effects and diffusion-limited processes. This result indicates that CuNi–PTC primarily stores charge through surface reactions, encompassing both double-layer capacitance and faradaic (pseudocapacitive) processes. The material's surface promotes rapid redox reactions, contributing to its high charge-storage capacity. While the surface-controlled processes dominate, there is some contribution from ion intercalation or diffusion into the electrode layers, though this is less significant compared to the surface capacitive effects. Additionally, the power law relationship (eqn (6)) was utilized to analyze the charge storage mechanisms in CuNi–PTC.

$$i_p = k_1 v + k_2 v^{\frac{1}{2}} \quad (6)$$

In this equation, i_p represents the peak current at a given potential, and v is the scan rate in V s^{-1}. The terms k_1v and $k_2v^{1/2}$ correspond to the contributions from surface capacitive effects and diffusion-controlled processes, respectively. To further investigate these contributions, a plot of $\frac{i_p}{v^{1/2}}$ *vs.* $v^{1/2}$ is generated (at 0.283 V in this case), where the slope and *y*-intercept from the linear fit yield the values for k_1 and k_2, respectively.[39] Fig. S4† illustrates the plot of $\frac{i_p}{v^{1/2}}$ *vs.* $v^{1/2}$ at 0.283 V. Fig. 5c presents a bar chart illustrating the surface current contributions at various scan rates. At a scan rate of 1 mV s^{-1}, the analysis showed that the diffusive current contributed 93.85%, while the capacitive contribution accounted for 6.15%. As the scan rate increased from 1 mV s^{-1} to 200 mV s^{-1}, the diffusive current contribution dropped significantly, from 93.85% to 51.89%. This indicates that at lower scan rates, the ions have sufficient time to diffuse into and out of the electrode, making diffusion the dominant charge storage mechanism. In contrast, at higher scan rates, ions do not have enough time to fully penetrate the material's bulk, resulting in charge storage being primarily controlled by rapid surface reactions, such as ion adsorption and fast redox processes occurring at or near the electrode surface.

Galvanostatic charge–discharge (GCD) curves are essential for assessing the specific capacitance of electrode materials, as they provide valuable information about the material's charge and discharge performance over time. Fig. 5d displays the GCD curves of CuNi–PTC recorded at different current densities within a potential range of 0.1 to 0.4 V. The non-linear shape of the GCD curves, which deviates from the ideal triangular profile typical of double-layer capacitors, confirms the pseudocapacitive nature of CuNi–PTC. At a current density of 1 A g^{-1}, CuNi–PTC exhibits a specific capacitance of 1066.24 F g^{-1}, highlighting its exceptional charge storage capacity. Moreover, CuNi–PTC achieves an energy density of 13.33 W h kg^{-1} and a power density of 150.03 W kg^{-1}, demonstrating its capability to store substantial energy and deliver it quickly. This combination makes CuNi–PTC well-suited for applications requiring both high energy and power densities.

Fig. 5e displays the Nyquist plot from electrochemical impedance spectroscopy (EIS) measurements, used to evaluate the charge transfer resistance (R_{ct}) of the electrode material. The plot shows that CuNi–PTC has an R_{ct} value of 2.42 Ω, indicating relatively low resistance and high conductivity, which facilitate efficient electron transfer during redox reactions. Additionally, long-term stability is a key consideration for the practical use of the as synthesized MOF as an electrode material. As shown in Fig. S5,† the material retains 94% of its initial capacitive performance even after 5000 charge–discharge cycles, demonstrating excellent cycling stability. This durability is crucial for the longevity and reliability of energy storage devices.

Thus, the charge storage behavior of CuNi–PTC can be understood as a hybrid process involving both pseudocapacitive and diffusion-controlled contributions, which vary with the scan rate. At lower scan rates, the diffusion-controlled processes dominate due to the sufficient time for ions to diffuse into the bulk of the electrode. This is indicative of intercalation or diffusion-limited redox reactions that occur deep within the material's structure. However, as the scan rate increases, there is a shift towards capacitive charge storage, driven by surface reactions and ion adsorption at the electrode surface. This transition is characteristic of materials exhibiting pseudocapacitance, where the charge storage primarily arises from fast reversible surface redox reactions. At higher scan rates, an almost equal balance between fast surface redox reactions and slower bulk diffusion is observed. This indicates that while the electrode surface facilitates rapid redox transitions, some ion access into the porous interior is still retained even at fast timescales. EIS further supports this, showing that CuNi–PTC offers low R_{ct}, indicating rapid electron transfer at the interface, while the Warburg region suggests that ion diffusion through the material's pores remains significant at lower scan rates.

To assess the structural integrity and morphological resilience of CuNi–PTC after extensive cycling, FESEM was performed following 5000 charge–discharge cycles. As depicted in Fig. S6,† the material retained its characteristic microstructure, with no significant collapse or fragmentation of the framework. Only slight surface roughening and minor aggregation were observed, indicating that the bimetallic CuNi–PTC architecture remains largely intact under prolonged cycling conditions. This

preservation of morphology highlights the excellent mechanical and electrochemical stability of the MOF, making it a promising candidate for long-term energy storage applications.

To better assess the performance of the CuNi–PTC electrode, Table S1† presents a comparison with recently reported bimetallic Ni-MOF based electrode materials used in supercapacitors. As is evident, the CuNi–PTC exhibits competitive or superior performance in terms of specific capacitance, and long-term stability, emphasizing the synergistic benefits of incorporating both Cu and Ni metal centers.

Fabrication of an asymmetric supercapacitor device

An asymmetric supercapacitor device was fabricated using CuNi–PTC (0.25 g) as the current collector, paired with activated carbon as the counter electrode and 3 M KOH as the electrolyte. Fig. 6a presents the cyclic voltammograms recorded across a potential range of 0–1.4 V at scan rates varying from 10 mV s^{-1} to 100 mV s^{-1}. The CV profiles exhibit a hybrid shape, falling between a rectangular form (indicative of pure electrical double-layer capacitance) and well-defined redox peaks (typical of strong faradaic reactions). Broad peaks and the observed symmetry around the zero-current axis suggest a pseudocapacitive behavior for the electrode material. This behavior arises from the combination of the pseudocapacitive characteristics of CuNi–PTC and the EDLC-dominant behavior of activated carbon.

The GCD curves, shown in Fig. 6b, recorded in the same potential range, display a nearly triangular shape with slight deviations from linearity, further confirming the pseudocapacitive nature of CuNi–PTC. The specific capacitance of CuNi–PTC in the two-electrode system was determined to be 606 F g^{-1} at a current density of 1 A g^{-1}. Additionally, the device delivered an energy density of 142.3 W h kg^{-1} and a power density of 2600 W kg^{-1}. EIS measurements (Fig. 6c) revealed an R_{ct} of 162.8 Ω. Moreover, the device demonstrated excellent cycling stability, retaining 95% of its initial capacitance after 5000 charge–discharge cycles (Fig. 6d).

Water splitting evaluation

CuNi–PTC was subsequently used as an electrocatalyst for both the hydrogen evolution reaction (HER) and the oxygen evolution reaction (OER) in water splitting. Fig. 7a and b show the linear sweep voltammetry (LSV) curves for the HER and OER, respectively. For HER, the MOF exhibits an overpotential of 212 mV at a current density of 10 mA cm^{-2}, indicating its efficiency in hydrogen production. This relatively low overpotential suggests

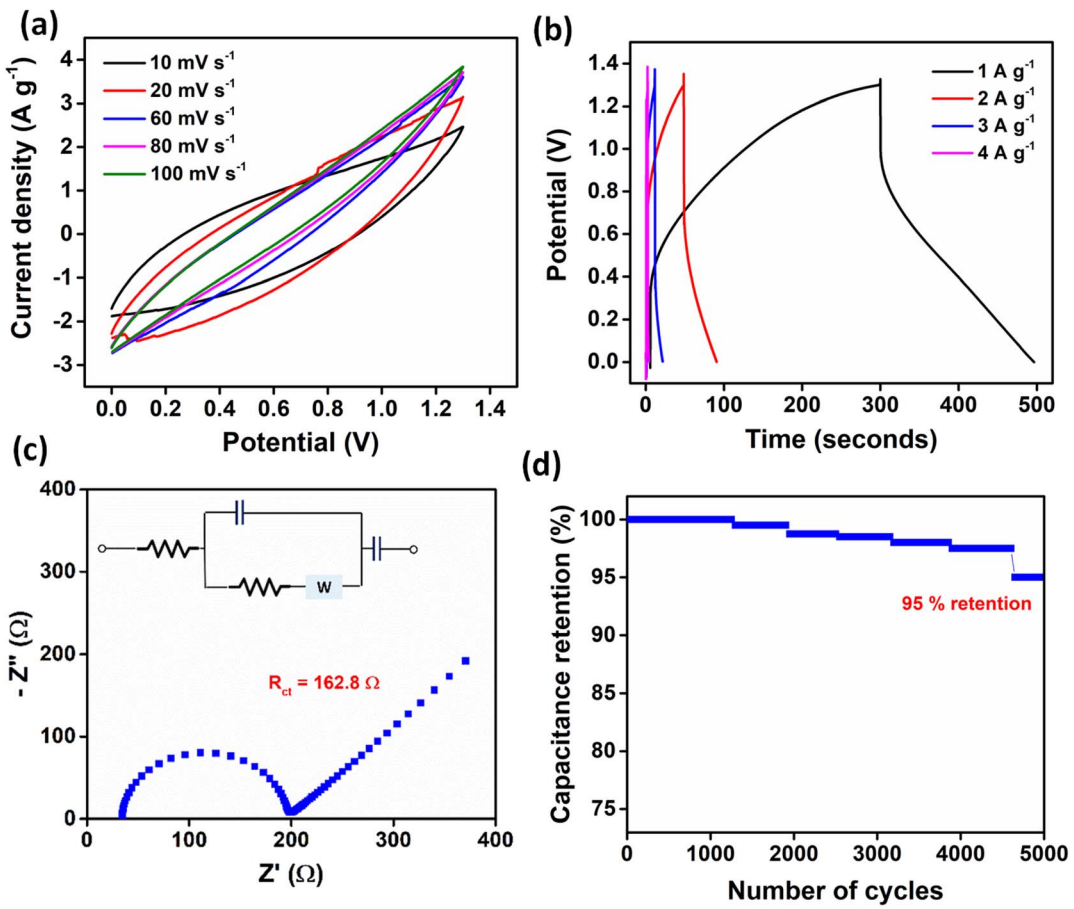

Fig. 6 (a) Cyclic voltammograms of CuNi–PTC at various scan rates, (b) GCD curves at different current densities, (c) Nyquist plot and (d) cycling stability of CuNi–PTC at current density 6 A g^{-1}, using a two-electrode system.

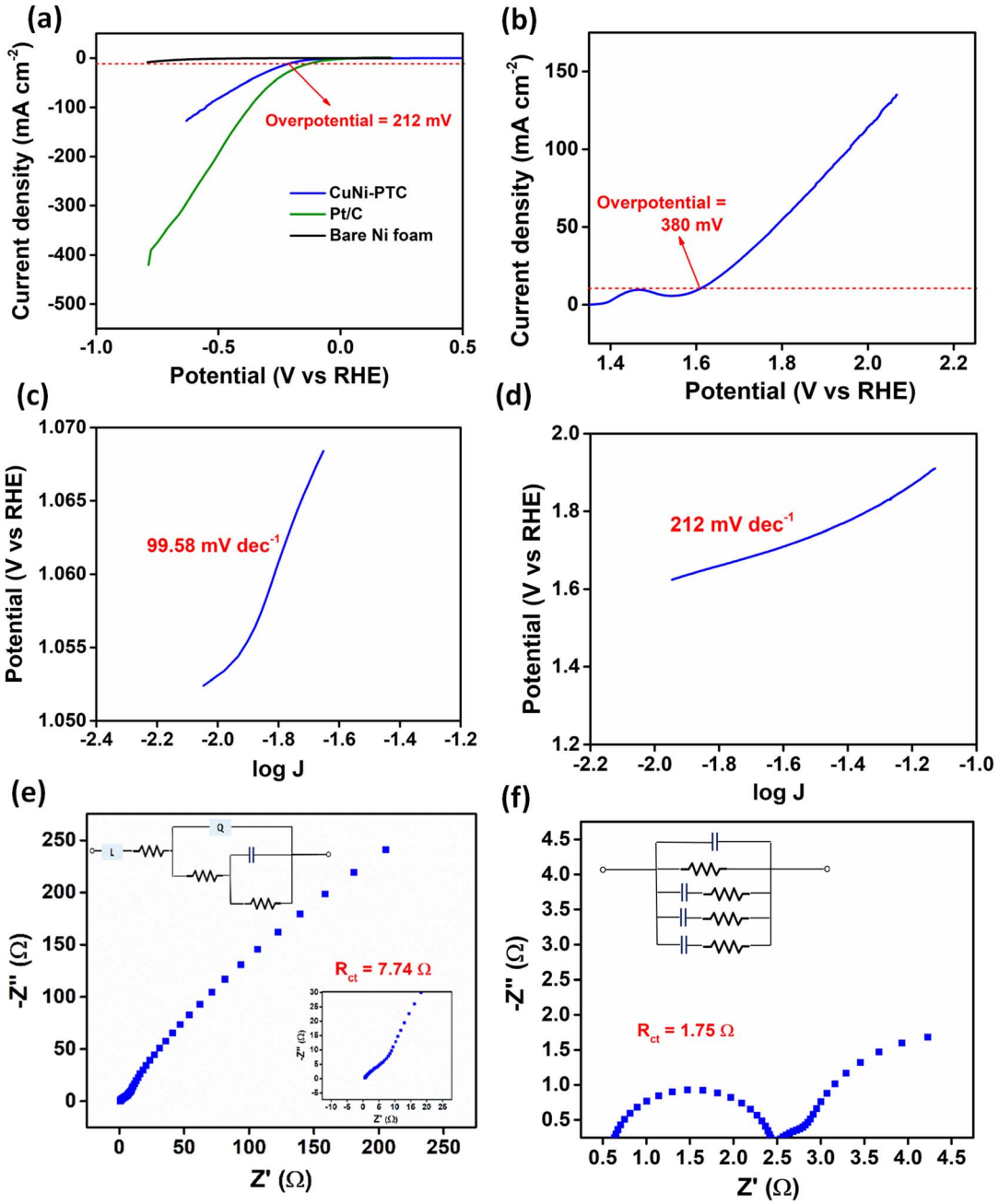

Fig. 7 (a and b) LSV curves, (c and d) Tafel plot and (e and f) Nyquist plots for HER and OER, respectively.

that CuNi–PTC effectively promotes proton reduction to hydrogen gas, minimizing energy consumption during the process. For OER, the MOF shows an overpotential of 380 mV at the same current density, demonstrating its ability to facilitate oxygen generation. Although the OER overpotential is higher than that of the HER, it still reflects good catalytic activity, as oxygen evolution typically involves greater kinetic challenges compared to the HER. Additionally, the LSV curve for overall water splitting, depicted in Fig. S7a,† shows that the overall reaction required a cell potential of 1.557 V at a current density of 10 mA cm^{-2}.

Tafel slopes help to clarify the mechanism and kinetics of hydrogen and oxygen evolution. In a basic medium, the HER mechanism starts with the Volmer step (eqn (7)), followed by either the Heyrovsky step (eqn (8)) or the Tafel step (eqn (9)), where * represents the active site. The corresponding Tafel slopes for these steps are approximately 120, 40, and 30 mV dec^{-1}, respectively.[40]

$$* + H_2O + e^- \rightarrow H^* + OH^- \quad (7)$$

$$* + H_2O + e^- + H^* \rightarrow H_2 + OH^- + * \quad (8)$$

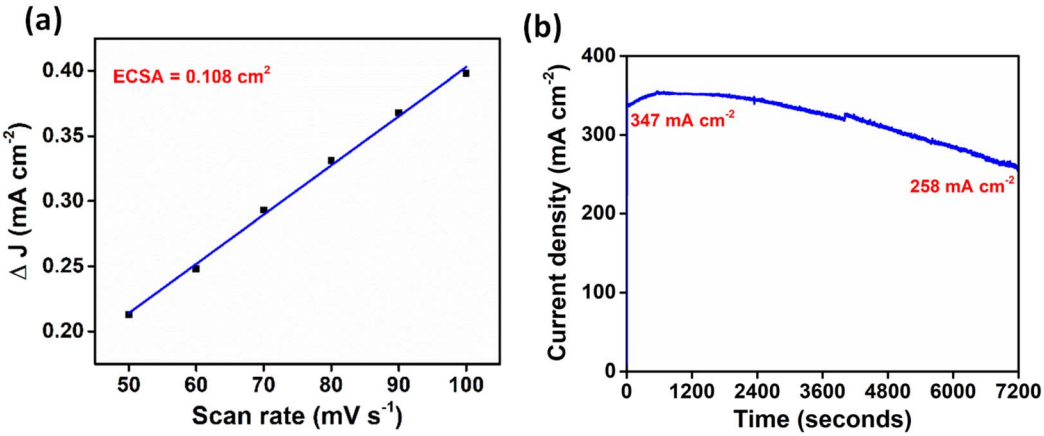

Fig. 8 (a) Linear plot of current density *vs.* scan rate. (b) stability test.

$$H^* + H^* \rightarrow H_2 + 2^* \quad (9)$$

The Tafel slope for the HER, measured at 99.58 mV dec^{-1}, suggests moderately fast reaction kinetics (Fig. 7c). This value indicates that hydrogen evolution on the synthesized MOF likely follows the Volmer–Heyrovsky mechanism, where proton adsorption is followed by an electron transfer step.[41] A Tafel slope in this range points to efficient electron transfer and a well-suited catalytic surface for hydrogen generation. For the OER, the Tafel slope is 212 mV dec^{-1}, reflecting slower kinetics compared to the HER (Fig. 7d). This higher value suggests that the OER mechanism involves multiple electron transfer steps with higher energy barriers, contributing to the slower reaction rate.[42]

Additionally, electrochemical impedance spectroscopy (EIS) was employed to assess the charge transfer resistance (R_{ct}) from the Nyquist plot, which indicates how easily electrons move across the electrode–electrolyte interface. The R_{ct} values were measured at 7.74 Ω for the HER and 1.75 Ω for the OER (Fig. 7e and f), suggesting that the CuNi–PTC MOF supports efficient electron transport at the interface. These low R_{ct} values highlight the material's good electrical conductivity and effective catalytic surface, ensuring efficient hydrogen and oxygen production.

To assess the electrochemical surface area (ECSA) of the electrode, non-faradaic CV curves were recorded over a scan rate range of 100 to 50 mV s^{-1} (Fig. S7b†). These curves were used to generate a linear plot of current density (ΔJ) *versus* the scan rate, which allowed for the determination of the double-layer capacitance (C_{dl}) of the electrode material. The ECSA was calculated using eqn (10), where C_s represents the specific capacitance of a smooth surface with an area of 1 cm^2. The C_s value for bare Ni foam is reported as 0.035 mF cm^{-2}.[43]

$$\mathrm{ECSA} = \frac{C_{dl}}{C_s} \quad (10)$$

Using this equation, the ECSA of CuNi–PTC was calculated to be 0.108 cm^2, reflecting the effective surface area available for electrochemical reactions (Fig. 8a). This value provides important insights into the electrode's performance during water splitting. The stability of CuNi–PTC as an electrocatalyst was further evaluated through bulk electrolysis over 2 hours (Fig. 8b). The MOF demonstrated fairly good stability, with a decrease in current density from 347 mA cm^{-2} to 258 mA cm^{-2}. The observed decrease in current density can be attributed to partial structural reorganization of the MOF surface under prolonged electrochemical conditions, as well as possible leaching from the electrode. Furthermore, the continuous evolution of gas bubbles may lead to the temporary blockage of active catalytic sites, thereby hindering efficient charge transfer.

To evaluate the structural and morphological stability of CuNi–PTC after prolonged electrochemical operation, post-catalysis characterization was performed following HER and OER testing. FESEM images (Fig. S8†) show that the MOF retained its overall morphology, with minor signs of surface roughening or aggregation. This suggests that the CuNi–PTC framework is structurally robust and resistant to degradation under the applied electrochemical conditions.

Conclusion

The synthesis and characterization of the CuNi–PTC MOF were thoroughly conducted. XRD analysis confirmed its crystalline structure, while FTIR and XPS confirmed the formation and bonding characteristics of the MOF. FESEM imaging revealed a combination of plate and flake-like morphology, and N_2 adsorption–desorption isotherms showcased a BET surface area of 28.25 m^2 g^{-1}. Electrochemical testing demonstrated that CuNi–PTC has a high specific capacitance of 1066.24 F g^{-1} at a current density of 1 A g^{-1}, along with commendable cycling stability, retaining 94% of its initial capacitance after 5000 charge–discharge cycles. Furthermore, the catalytic performance of CuNi–PTC for both the HER and OER was assessed, showing overpotentials of 212 mV for the HER and 380 mV for the OER at a current density of 10 mA cm^{-2} and exhibiting good long-term stability.

Data availability

The data supporting this article have been included as part of the ESI.†

Author contributions

Samika Anand: investigation, methodology, conceptualization, data curation, formal analysis, writing-original draft. Kalathiparambil Rajendra Pai Sunajadevi: resources, supervision, conceptualization, project administration, validation, writing-review & editing.

Conflicts of interest

The authors declare that they have no known competing financial interests or personal relationships that could have appeared to influence the work reported in this paper.

Acknowledgements

The authors acknowledge the support of Central Instrumentation Facility (CIF), Christ University, Bangalore. Samika Anand is grateful to the Department of Science and Technology, Government of India, for providing INSPIRE fellowship.

References

1 I. Hadjipaschalis, A. Poullikkas and V. Efthimiou, Overview of current and future energy storage technologies for electric power applications, *Renew. Sustain. Energy Rev.*, 2009, **13**, 1513–1522.
2 E. Sayed, A. Olabi, A. Alami, A. Radwan, A. Mdallal, A. Rezk and M. Abdelkareem, Renewable Energy and Energy Storage Systems, *Energies*, 2023, **16**, 1415.
3 J. Mitali, S. Dhinakaran and A. A. Mohamad, Energy storage systems: a review, *Energy Storage Sav.*, 2022, **1**, 166–216.
4 M. Yaseen, M. A. K. Khattak, M. Humayun, M. Usman, S. S. Shah, S. Bibi, B. S. U. Hasnain, S. M. Ahmad, A. Khan, N. Shah, A. A. Tahir and H. Ullah, A Review of Supercapacitors: Materials Design, Modification, and Applications, *Energies*, 2021, **14**, 7779.
5 Y. Zhang, Z. Li, S. He, Y. Qiao, A. Yuan, J. Wu and H. Zhou, Interfacial engineering of heterostructured CoP/FeP nanoflakes as bifunctional electrocatalyts toward alkaline water splitting, *J. Colloid Interface Sci.*, 2025, **679**, 20–29.
6 H. Sun, X. Xu, H. Kim, W. Jung, W. Zhou and Z. Shao, Electrochemical Water Splitting: Bridging the Gaps Between Fundamental Research and Industrial Applications, *Energy Environ. Mater.*, 2023, **6**(5), e12441.
7 G. Dey, Shadab and A. Aijaz, Metal-Organic Framework Derived Nanostructured Bifunctional Electrocatalysts for Water Splitting, *ChemElectroChem*, 2021, **8**, 3782–3803.
8 C. Chen, J. Li, Z. Lv, M. Wang and J. Dang, Recent strategies to improve the catalytic activity of pristine MOFs and their derived catalysts in electrochemical water splitting, *Int. J. Hydrogen Energy*, 2023, **48**, 30435–30463.
9 N. Raza, T. Kumar, V. Singh and K.-H. Kim, Recent advances in bimetallic metal-organic framework as a potential candidate for supercapacitor electrode material, *Coord. Chem. Rev.*, 2021, **430**, 213660.
10 R. Zahid, M. R. A. Karim, M. W. Khan and M. A. Marwat, Electrocatalytic water splitting: a review under the shade of metal-organic frameworks, *Int. J. Hydrogen Energy*, 2024, **57**, 958–982.
11 H.-C. J. Zhou and S. Kitagawa, Metal–Organic Frameworks (MOFs), *Chem. Soc. Rev.*, 2014, **43**, 5415–5418.
12 M. Ding, X. Cai and H.-L. Jiang, Improving MOF stability: approaches and applications, *Chem. Sci.*, 2019, **10**, 10209–10230.
13 Y. Peng, S. Sanati, A. Morsali and H. García, Metal–Organic Frameworks as Electrocatalysts, *Angew. Chem., Int. Ed.*, 2023, **62**(9), e202214707.
14 S. Sanati, A. Morsali and H. García, First-row transition metal-based materials derived from bimetallic metal–organic frameworks as highly efficient electrocatalysts for electrochemical water splitting, *Energy Environ. Sci.*, 2022, **15**, 3119–3151.
15 S. Sanati, Q. Wang, R. Abazari and M. Liu, Recent advanced strategies for bimetallenes toward electrocatalytic energy conversion reactions, *Chem. Commun.*, 2024, **60**, 3129–3137.
16 A. Zulys, D. Asrianti and J. Gunlazuardi, Light-Harvesting Metal-Organic Frameworks (MOFs) La-PTC for Photocatalytic Dyes Degradation, *Bull. Chem. React. Eng. Catal.*, 2021, **16**(1), 020035.
17 M. Majumder, P. Sheath, J. I. Mardel, T. G. Harvey, A. W. Thornton, A. Gonzago, D. F. Kennedy, I. Madsen, J. W. Taylor, D. R. Turner and M. R. Hill, Aqueous Molecular Sieving and Strong Gas Adsorption in Highly Porous MOFs with a Facile Synthesis, *Chem. Mater.*, 2012, **24**, 4647–4652.
18 Z. Xing, Z. Jian, W. Luo, Y. Qi, C. Bommier, E. S. Chong, Z. Li, L. Hu and X. Ji, A perylene anhydride crystal as a reversible electrode for K-ion batteries, *Energy Storage Mater.*, 2016, **2**, 63–68.
19 J. Zhao, P. Su, Y. Zhao, M. Li, Y. Yang, Q. Yang and C. Li, Systematic morphology and phase control of Mg-ptcda coordination polymers by Ostwald ripening and self-templating, *J. Mater. Chem.*, 2012, **22**, 8470–8475.
20 Z. Wei, H. Qiao, H. Yang, C. Zhang and X. Yan, Characterization of NiO nanoparticles by anodic arc plasma method, *J. Alloys Compd.*, 2009, **479**, 855–858.
21 S. Suresh, S. Karthikeyan and K. Jayamoorthy, FTIR and multivariate analysis to study the effect of bulk and nano copper oxide on peanut plant leaves, *J. Sci. Adv. Mater. Devices*, 2016, **1**, 343–350.
22 L. C. Christina, J. Gunlazuardi and A. Zulys, Synthesis and characterization of lanthanide metal-organic framework with perylene 3,4,9,10-tetracarboxylate ligand, *IOP Conf. Ser.: Mater. Sci. Eng.*, 2020, **902**(1), 012046.
23 S. Nzikayel, I. J. Akpan and E. C. Adams, Synthesis, FTIR and Electronic Spectra Studies of Metal (II) Complexes of Pyrazine-2-Carboxylic Acid Derivative, *Med. Chem.*, 2017, **7**(11), 321–323.
24 S. Anand and K. R. Sunaja Devi, Optimizing malachite green adsorption with Co-PTC metal organic framework: insights into mechanisms and performance, *J. Mol. Struct.*, 2024, **1318**, 139256.

25 L. A. Saghatforoush, F. Chalabian, A. Aminkhani, G. Karimnezhad and S. Ershad, Synthesis, spectroscopic characterization and antibacterial activity of new cobalt(II) complexes of unsymmetrical tetradentate (OSN2) Schiff base ligands, *Eur. J. Med. Chem.*, 2009, **44**, 4490–4495.

26 A. K. Sharma, S. Desnavi, C. Dixit, U. Varshney and A. Sharma, Extraction of Nickel Nanoparticles from Electroplating Waste and Their Application in Production of Bio-diesel from Biowaste, *Int. J. Chem. Eng. Appl.*, 2015, **6**, 156–159.

27 M. Elango, M. Deepa, R. Subramanian and A. M. Musthafa, Synthesis, Characterization, and Antibacterial Activity of Polyindole/Ag–Cuo Nanocomposites by Reflux Condensation Method, *Polym. Plast. Technol. Eng.*, 2018, **57**, 1440–1451.

28 G. Simões dos Reis, C. M. Subramaniyam, A. D. Cárdenas, S. H. Larsson, M. Thyrel, U. Lassi and F. García-Alvarado, Facile Synthesis of Sustainable Activated Biochars with Different Pore Structures as Efficient Additive-Carbon-Free Anodes for Lithium- and Sodium-Ion Batteries, *ACS Omega*, 2022, **7**, 42570–42581.

29 S. Jing, X. Gong, S. Ji, L. Jia, B. G. Pollet, S. Yan and H. Liang, Self-standing heterostructured NiC x -NiFe-NC/biochar as a highly efficient cathode for lithium–oxygen batteries, *Beilstein J. Nanotechnol.*, 2020, **11**, 1809–1821.

30 C. J. Oluigbo, Y. Xu, H. Louis, A. B. Yusuf, W. Yaseen, N. Ullah, K. J. Alagarasan, M. Xie, E. E. Ekpenyong and J. Xie, Controllable fabrication of abundant nickel-nitrogen doped CNT electrocatalyst for robust hydrogen evolution reaction, *Appl. Surf. Sci.*, 2021, **562**, 150161.

31 J. Jiang, X. X. Liu, J. Han, K. Hu and J. S. Chen, Self-Supported Sheets-on-Wire CuO@Ni(OH)2/Zn(OH)2 Nanoarrays for High-Performance Flexible Quasi-Solid-State Supercapacitor, *Processes*, 2021, **9**, 680.

32 A. Roy, A. K. Mukhopadhyay, S. C. Das, G. Bhattacharjee, A. Majumdar and R. Hippler, Surface Stoichiometry and Optical Properties of Cux–TiyCz Thin Films Deposited by Magnetron Sputtering, *Coatings*, 2019, **9**, 551.

33 J. Wei, Y. Li, D. Dai, F. Zhang, H. Zou, X. Yang, Y. Ji, B. Li and X. Wei, Surface Roughness: A Crucial Factor To Robust Electric Double Layer Capacitors, *ACS Appl. Mater. Interfaces*, 2020, **12**, 5786–5792.

34 F. Ambroz, T. J. Macdonald, V. Martis and I. P. Parkin, Evaluation of the BET Theory for the Characterization of Meso and Microporous MOFs, *Small Methods*, 2018, **2**(11), 1800173.

35 J. Y. Kim, J. Kang, S. Cha, H. Kim, D. Kim, H. Kang, I. Choi and M. Kim, Stability of Zr-Based UiO-66 Metal–Organic Frameworks in Basic Solutions, *Nanomaterials*, 2024, **14**, 110.

36 T. He, X.-J. Kong and J.-R. Li, Chemically Stable Metal–Organic Frameworks: Rational Construction and Application Expansion, *Acc. Chem. Res.*, 2021, **54**, 3083–3094.

37 T. Devic and C. Serre, High valence 3p and transition metal based MOFs, *Chem. Soc. Rev.*, 2014, **43**, 6097–6115.

38 M. Z. Iqbal, M. M. Faisal, S. R. Ali, S. Farid and A. M. Afzal, Co-MOF/polyaniline-based electrode material for high performance supercapattery devices, *Electrochim. Acta*, 2020, **346**, 136039.

39 K. Karuppasamy, D. Vikraman, S. Hussain, P. Santhoshkumar, R. Bose, P. Sivakumar, A. Alfantazi, J. Jung and H. Kim, Unveiling the Redox Electrochemistry of MOF-Derived fcc-NiCo@GC Polyhedron as an Advanced Electrode Material for Boosting Specific Energy of the Supercapattery, *Small*, 2022, **2**(18), 2107284.

40 A. Alobaid, C. Wang and R. A. Adomaitis, Mechanism and Kinetics of HER and OER on NiFe LDH Films in an Alkaline Electrolyte, *J. Electrochem. Soc.*, 2018, **165**, J3395–J3404.

41 K. Nayana and A. P. Sunitha, MoS2−x/GCD-MoS2−x nanostructures for tuning the overpotential of Volmer-Heyrovsky reaction of electrocatalytic hydrogen evolution, *Int. J. Hydrogen Energy*, 2024, **55**, 422–431.

42 L. Tang, T. Fan, Z. Chen, J. Tian, H. Guo, M. Peng, F. Zuo, X. Fu, M. Li, Y. Bu, Y. Luo, J. Li and Y. Sun, Binary-dopant promoted lattice oxygen participation in OER on cobaltate electrocatalyst, *Chem. Eng. J.*, 2021, **417**, 129324.

43 M. Ramachandra and S. D. Kalathiparambil Rajendra Pai, Exploring the potential application of Cr2AlC MAX phase as an emerging electrocatalyst for overall water splitting, *Emergent Mater.*, 2024, DOI: **10.1007/s42247-024-00815-w**.